Conductive shield for ultra-low-field magnetic resonance imaging: Theory and measurements of eddy currents

Koos C. J. Zevenhoven, Sarah Busch, Michael Hatridge, Fredrik Öisjöen, Risto J. Ilmoniemi, and John Clarke

Citation: Journal of Applied Physics **115**, 103902 (2014); doi: 10.1063/1.4867220
View online: http://dx.doi.org/10.1063/1.4867220
View Table of Contents: http://scitation.aip.org/content/aip/journal/jap/115/10?ver=pdfcov
Published by the AIP Publishing

Conductive shield for ultra-low-field magnetic resonance imaging: Theory and measurements of eddy currents

Koos C. J. Zevenhoven,[1,2,a)] Sarah Busch,[1,b)] Michael Hatridge,[1,c)] Fredrik Öisjöen,[1,3,d)] Risto J. Ilmoniemi,[2] and John Clarke[1]
[1]*Department of Physics, University of California, Berkeley, California 94720-7300, USA*
[2]*Department of Biomedical Engineering and Computational Science, Aalto University School of Science, FI-00076 Aalto, Finland*
[3]*Department of Microtechnology and Nanoscience – MC2, Chalmers University of Technology, SE-412 96 Göteborg, Sweden*

(Received 19 December 2013; accepted 19 February 2014; published online 11 March 2014)

Eddy currents induced by applied magnetic-field pulses have been a common issue in ultra-low-field magnetic resonance imaging. In particular, a relatively large prepolarizing field—applied before each signal acquisition sequence to increase the signal—induces currents in the walls of the surrounding conductive shielded room. The magnetic-field transient generated by the eddy currents may cause severe image distortions and signal loss, especially with the large prepolarizing coils designed for *in vivo* imaging. We derive a theory of eddy currents in thin conducting structures and enclosures to provide intuitive understanding and efficient computations. We present detailed measurements of the eddy-current patterns and their time evolution in a previous-generation shielded room. The analysis led to the design and construction of a new shielded room with symmetrically placed 1.6-mm-thick aluminum sheets that were weakly coupled electrically. The currents flowing around the entire room were heavily damped, resulting in a decay time constant of about 6 ms for both the measured and computed field transients. The measured eddy-current vector maps were in excellent agreement with predictions based on the theory, suggesting that both the experimental methods and the theory were successful and could be applied to a wide variety of thin conducting structures. © *2014 AIP Publishing LLC*. [http://dx.doi.org/10.1063/1.4867220]

I. INTRODUCTION

Magnetic resonance imaging (MRI) is widely used clinically to image any part of the human body with superb spatial resolution. It is based on nuclear magnetic resonance (NMR), almost always of hydrogen nuclei (protons). The magnetization $\vec{M}_H$ of the ensemble of protons precesses around the magnetic field $\vec{B}$ at the Larmor frequency $f_L = \gamma B$, where $\gamma = 42.58\,\mathrm{MHz/T}$ is the proton gyromagnetic ratio.[1] For a typical main field $B_0 = 3\,\mathrm{T}$, $f_L = 127\,\mathrm{MHz}$. The precessing magnetic moment induces into an induction coil an oscillating voltage, which is amplified and recorded for subsequent processing. Spatial information is encoded into the signal by pulsed gradient fields that define the NMR frequency voxel-by-voxel in three-dimensional space.

Despite the trend to higher imaging fields in clinical scanners, in recent years there has been growing interest in ultra-low-field MRI (ULF MRI),[2] in which B_0 is typically on the order of only 100 μT. In addition to lower cost, lower weight, reduced patient confinement, and silent operation, potential advantages of ULF MRI include higher intrinsic contrast between different tissues[3] and various novel imaging techniques.[4–8] The combination of ULF MRI with magnetoencephalography (MEG)—which detects weak magnetic fields generated by neuronal activity in the brain—has emerged as a new field of substantial interest.[9,10]

The four-order-of-magnitude reduction in B_0 produces the same reduction in both M_H and f_L. Since the voltage induced in the detection coil scales with frequency, the detected signal from the coil scales as B_0^2. The enormous loss in signal amplitude at ULF compared with the high-field amplitude is overcome in two ways. First, the application of a prepolarizing magnetic field $B_p \gg B_0$ before initiating the imaging sequence produces a magnetization M_H that is independent of B_0. Second, one detects the NMR signal with an untuned superconducting input circuit inductively coupled to a Superconducting QUantum Interference Device (SQUID)[11] which, in contrast to a conventional receiver coil, has a frequency-independent response. Consequently, the sensitivity of the SQUID-based detector does not fall off as f_L is lowered. The combination of prepolarization and SQUID detection results in a detected signal amplitude that is independent of B_0.

To increase the signal-to-noise ratio of the measurement, one chooses B_p to be as large as practical, for example, 10–150 mT, and attempts to reduce the measurement noise referred to the superconducting pickup loop coupled to the SQUID to the lowest level possible. Minimizing the detector noise generally necessitates a shielded room to exclude both radio-frequency (RF) interference and magnetic noise in the

[a)]Electronic mail: koos.zevenhoven@aalto.fi
[b)]Current address: NASA, Goddard Space Flight Center, Greenbelt, Maryland 20771, USA.
[c)]Current address: Department of Applied Physics, Yale University, New Haven, Connecticut 06511, USA.
[d)]Current address: Awapatent AB, S. Hamngatan 37-41, SE-404 28 Göteborg, Sweden.

signal bandwidth. The combination of the relatively high, pulsed B_p and the shielded room, however, presents a dilemma: the large magnetic pulse induces eddy currents into the shield, producing transient fields that may both distort $\vec{B}_0$ and delay the time at which the SQUID can be locked to acquire data, thus reducing the signal-to-noise ratio substantially.

Eddy-current transients have proven to be a common issue impeding the development of ULF MRI.[8,10,12] Broadly speaking, there are three solutions to this problem. One is to cancel the magnetic field from the polarizing coil by means of a self-shielded coil design[10,13] or additional coils at the shielded-room walls.[14,15] Another solution is to control the eddy currents with a specifically designed current waveform fed into another coil.[16] The third approach is to reduce the decay times of the eddy currents to a level at which the transient magnetic field becomes negligible when the image encoding sequence is initiated. The last approach is described in this paper.

There are two styles of shielded room. For MEG, which requires very low noise at frequencies down to below 1 Hz, the magnetically shielded room (MSR) is made of a high-permeability (μ) alloy such as μ metal[17] ($\mu \sim 10^4 \mu_0$, where μ_0 is the permeability of free space). Such materials offer a low-reluctance path for magnetic flux, guiding the flux lines around the interior of the MSR at frequencies down to zero. Often, μ metal is combined with layers of aluminum with welded seams[18] for added shielding and for better mechanical properties.[19] For ULF MRI, one does not require a high level of rejection of time-varying magnetic fields at frequencies well below f_L, and the earth's static magnetic field can be canceled using current-carrying coils. Consequently, the MSR can be made entirely of aluminum, enabling one to construct a shielded room which is vastly cheaper and lighter than a μ-metal room. In a conductive shield, external fluctuating fields induce eddy currents in the metal, giving rise to magnetic fields that tend to cancel the incident fields. This cancellation, which vanishes for static fields, increases with frequency.

In this paper, we study the purely conducting MSR. We examine the physical nature of the eddy-current problem theoretically and experimentally. We introduce a methodology to eliminate eddy-current modes with high inductances and low resistances in our shielded room to reduce the decay times of the eddy currents to a level at which we can perform *in vivo* ULF MRI. In Sec. II, we briefly describe our ULF MRI system and the previous aluminum room. Section III contains a detailed theory for eddy currents, and Sec. IV describes the design and construction of a new aluminum room that reduces the eddy current transients to an acceptable level. In Sec. V, we describe our methods to measure vector maps of the eddy currents and the magnetic field transients produced by switching off B_p. In Sec. VI, we present experimental results for both the previous and new room and compare our results with theoretical predictions. Section VII contains our conclusions and outlook.

II. ULTRA-LOW-FIELD MRI SYSTEM

The Berkeley ULF MRI system involves the coils shown in Fig. 1(a). Around the cubic structure are two pairs of square coils, 1.8 m on a side, that cancel the x and y components of the earth's field. The horizontal B_0 coil, which reinforces the z component of the earth's field to a total of about 130 μT, and encoding gradient coils consist of pairs of planar coils parallel to the xy plane. The polarizing coil [Fig. 1(b)] is placed under the low-noise dewar,[20] close to the lowest loop of the second-order, superconducting gradiometer coupled to the SQUID. The wire-wound gradiometer rejects uniform applied fields by a factor of about 1000, yielding a high attenuation of noise from distant noise sources. The entire assembly is surrounded by a shield that, in the previous-generation system, had dimensions of $2.4 \times 2.4 \times 2.4\,\mathrm{m}^3$ ($8^3\,\mathrm{ft}^3$) [Fig. 1(c)]. The 6.4-mm-thick plates were bolted tightly to a frame made of square, hollow aluminum bars, using a large number of brass bolts. This shield provided some attenuation at 60 Hz, and substantial attenuation at the 5.6-kHz NMR frequency.

The polarizing coil, designed for *in vivo* imaging, consists of 240 tightly packed circular turns of copper pipe, with a $4 \times 4\,\mathrm{mm}^2$ square cross section. The height is 115 mm, and the inner and outer radii are 163 mm and 208 mm, respectively. Water flowing through the pipe enables the coil to be operated in the pulsed mode indefinitely. A 200-A current pulse produces an axial field $B_p \approx 150$ mT at the midplane of the coil, corresponding to a magnetic dipole moment of $5.4\,\mathrm{kAm}^2$. The current, supplied by a 25-kW power supply, is ramped[21] to zero as a quarter cosine wave (0 to $\pi/2$) in 10 ms. With the 6.4-mm shield, when the current became zero, a transient field greater than 150 μT remained at the detector, decaying roughly exponentially with a time constant of 50 ms. The magnitude and time constant of this field are unacceptably large for ULF MRI. This realization led us to develop a new aluminum shield with a greatly reduced transient field magnitude and decay time, yet with sufficient shielding at the NMR frequency.

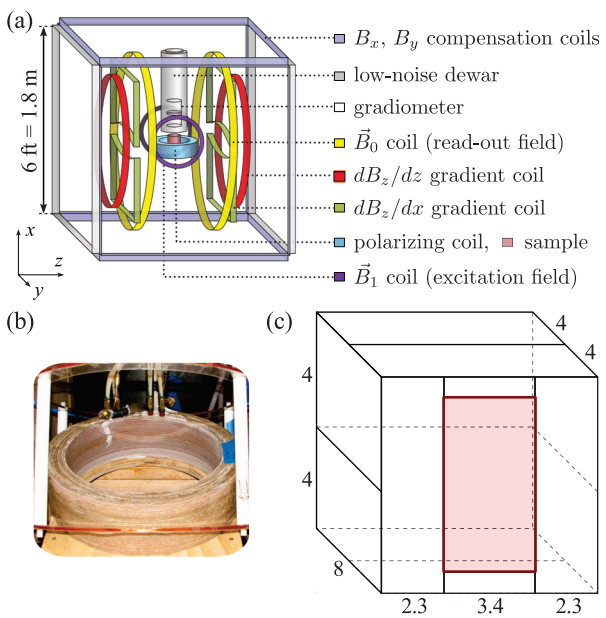

FIG. 1. ULF MRI system. (a) Coil system (dB_z/dy coil omitted for clarity), (b) new water-cooled polarizing coil, and (c) configuration of 6.4-mm aluminum plates in the old MSR (dimensions in feet = 0.3048 m). Shaded rectangle is the door.

III. THEORY

At very high frequencies (short wavelengths), electromagnetic waves are reflected and absorbed by conductive sheets. Shielding against radio-frequency interference is, in principle, straightforward in that even a single thin layer, such as household aluminum foil, can provide efficient shielding. The difficulty, however, is that electromagnetic radiation leaks through seams and holes and can be transferred to inside the MSR by wires acting as receiving and transmitting antennas. To solve these issues, pass-throughs for signals, currents and coolants need to be designed and implemented carefully, and all seams must be conductively bridged.

The electrodynamics between RF and the kHz frequencies of ULF MRI is complicated. At the low-frequency end, time-varying magnetic fields induce eddy currents into conductors according to Faraday's law and Ohm's law, and these currents produce magnetic fields according to the Biot–Savart law. Besides shielding, this leads to transient magnetic fields after ULF MRI pulses. For shielding at very low frequencies, these decay times are long and comparable to the pulse sequences.[16]

Most of the inductive energy held by the eddy currents is dissipated within the shield by its resistance. First, as a highly simplified model, we consider the eddy currents in the shield as an electrical circuit with resistance R and inductance L. The current I in the circuit as a function of time t is governed by Kirchhoff's second law

$$L\frac{d}{dt}I(t) + RI(t) + \mathcal{E}(t) = 0, \tag{1}$$

where $\mathcal{E}$ is an induced electromotive force (EMF) that transfers energy into (or out of) the system. For example, when the polarizing coil, with mutual inductance M with the eddy-current circuit, is pulsed with a current $I_p(t)$, $\mathcal{E} = MdI_p/dt$. Immediately after the pulse (at $t=0$), the magnitude of the eddy current, given by setting $\mathcal{E} = 0$ in Eq. (1), decays as $e^{-t/\tau}$, where $\tau = L/R$.

A related concept is the inductor-resistor (LR) low-pass filter, with a response as a function of angular frequency ω given by the frequency-domain solution of Eq. (1)

$$R\hat{I}(\omega) = -\frac{1}{1+i\tau\omega}\hat{\mathcal{E}}(\omega), \tag{2}$$

where $\hat{}$ denotes the temporal Fourier transform. Here, $-\mathcal{E}$ and RI are the input and output voltages, respectively. The roll-off frequency of the filter is $f_c = \omega_c/2\pi = 1/2\pi\tau$.

Since the shielding provided by a conductive MSR is related to the LR low-pass filter, there is a trade-off between shielding and eddy-current properties: decreasing the resistance R of the shield increases τ and improves the shielding, but also lengthens the harmful eddy-current transient.

In reality, however, a better model is required to understand and predict the behavior of induced eddy currents satisfactorily. In this section, we construct a theoretical model for a thin conductive shield, with the eddy currents considered as an infinite number of LR circuits.

A. Surface currents in a thin shield

Consider a thin-wall MSR, represented by a piecewise smooth surface S enclosing volume V, with an outer normal vector $\hat{n}(\vec{r})$ at $\vec{r} \in S$. Provided a surface current density $\vec{K}$ adequately describes the currents in the MSR, the system becomes essentially two-dimensional and thus simple to understand and analyze. However, not all surface current density patterns are physically reasonable. At low frequencies, Maxwell's displacement current $\mu_0\epsilon_0\partial\vec{E}/\partial t$ is negligible; here, $\vec{E}$ is the electric field and ϵ_0 the permittivity of free space. Ampère's law

$$\nabla \times \vec{B} = \mu_0\vec{J} \tag{3}$$

is then valid. Taking its divergence yields $\nabla \cdot \vec{J} = 0$, implying that the current density $\vec{J}$ consists of circulating (eddy) currents only.

Further assuming that the eddy currents in S are tangent to S, one can write the boundary condition for the magnetic field across S as

$$\vec{B}_+(\vec{r}) - \vec{B}_-(\vec{r}) = \mu_0\vec{K}(\vec{r}) \times \hat{n}(\vec{r}), \tag{4}$$

which follows from the integral form of Eq. (3). The subscripts $+$ and $-$ denote limits taken from outside and inside V, respectively. Assuming a layer of space with $\vec{J} = 0$ around S, one can write the magnetic fields in Eq. (4) using scalar potentials $\Phi_\pm$ as $\vec{B}_+ = -\mu_0\nabla\Phi_+$ and $\vec{B}_- = -\mu_0\nabla\Phi_-$, yielding

$$\vec{K} \times \hat{n} = -\nabla(\Phi_+ - \Phi_-) = -\nabla\Psi, \tag{5}$$

where $\Psi = \Phi_+ - \Phi_-$. Since $\vec{K}$ is tangential, this leads to

$$\vec{K} = \nabla\Psi \times \hat{n}. \tag{6}$$

Clearly, $\vec{K}$ is independent of $\nabla\Psi \cdot \hat{n}$, and $\vec{K}$ is thus fully described by a scalar function Ψ defined in S. A further observation based on Eq. (6) is that the eddy currents flow along isocontours of Ψ in S. The scalar representation of eddy currents significantly facilitates theoretical analysis and is a generalization of the stream functions used in 2-D fluid dynamics on a plane[22] and in the design of cylindrical MRI gradient coils.[23]

While we have shown that any tangential surface current density $\vec{K}$ can be represented using a scalar function Ψ, it is still unclear whether all (piecewise) differentiable functions Ψ correspond to possible eddy-current patterns. To examine this issue, consider any Ψ and a subset S_s of S. The current flowing into S_s through its boundary ∂S_s is given by

$$\oint_{\partial S_s} \vec{K} \cdot \hat{n} \times d\vec{l} = \oint_{\partial S_s} \vec{K} \times \hat{n} \cdot d\vec{l} = -\oint_{\partial S_s} \nabla\Psi \cdot d\vec{l} = 0, \tag{7}$$

where $d\vec{l}$ is a differential path element. Here, we have rearranged the scalar triple product and used Eq. (5); thus, no net current flows into S_s. Since S_s is arbitrary, there is no region in S that accumulates charge, and $\vec{K} = \nabla\Psi \times \hat{n}$ is indeed a possible eddy-current pattern.

B. Eddy-current basis functions as electric circuits

The scalar representation introduced above is convenient for studying the behavior of eddy currents in the shield. When the scalar function is expressed in a suitable function basis, the dynamics of the system can be modeled by a coupled system in this basis. We assume that the eddy-current pattern in S is given in terms of scalar basis functions ψ_k so that $\Psi = \sum_k j_k \psi_k$ and

$$\vec{K}(\vec{r},t) = \sum_k j_k(t) \nabla\psi_k(\vec{r}) \times \hat{n}(\vec{r}) = \sum_k j_k(t) \vec{\kappa}_k(\vec{r}), \quad (8)$$

where $\vec{\kappa}_k(\vec{r}) = \nabla\psi_k \times \hat{n}$ and $\nabla\psi_k \cdot \hat{n} = 0$. We begin by defining concepts and quantities analogous to those of electric circuits to facilitate further analysis.

From Eq. (8), the coefficient j_k can be interpreted as the current in circuit k. However, to have meaningful circuit quantities such as resistance and inductance, the basis must be normalized. We approach the normalization problem by considering the ohmic power dissipated in the circuit, which would preferably take the form $R_k j_k^2$, where R_k is the resistance of the circuit. On the other hand, the power per unit area dissipated by surface current density $\vec{K}$ at $\vec{r}$ in S is $K^2(\vec{r})/\sigma(\vec{r})d(\vec{r})$, where σ and d are the conductivity and thickness of the shield, respectively. Thus, for $\vec{K} = j_k\vec{\kappa}_k$, the ohmic power dissipation is

$$P = R_k j_k^2 = j_k^2 \oint_S \frac{\kappa_k^2(\vec{r})}{\sigma(\vec{r})d(\vec{r})} dS. \quad (9)$$

Now, if σd is independent of $\vec{r}$, one obtains $R_k = (\sigma d)^{-1} \oint_S \kappa_k^2 \, dS$. Choosing the normalization condition[24]

$$\oint_S \kappa_k^2 \, dS = \oint_S (\nabla\psi_k)^2 \, dS = 1 \quad (10)$$

conveniently leads to $R_k = (\sigma d)^{-1}$, also known as the sheet resistance, and in the general case, to

$$R_k = \oint_S \frac{\kappa_k^2(\vec{r})}{\sigma(\vec{r})d(\vec{r})} dS. \quad (11)$$

With these definitions, R_k and j_k have the proper dimensions of resistance and current.

We now consider the self-inductive energy of circuit k, preferably given by $\frac{1}{2}L_k j_k^2$, where L_k is the inductance of the circuit. As with the dissipated power, the inductive energy can be expressed as a surface integral since the energy per unit area of a surface current $\vec{K}$ is given by $\frac{1}{2}\vec{A}\cdot\vec{K}$, where $\vec{A}$ is the vector potential produced by $\vec{K}$. If $\vec{K} = j_k\vec{\kappa}_k$ and $\vec{A} = j_k\vec{a}_k$, where $\vec{a}_k$ is the vector potential generated by a unit current $\vec{\kappa}_k$, one obtains

$$\frac{1}{2}L_k j_k^2 = \frac{1}{2}\oint_S \vec{A}\cdot\vec{K}\, dS = \frac{j_k^2}{2}\oint_S \vec{a}_k \cdot \vec{\kappa}_k \, dS. \quad (12)$$

This directly leads to an expression for L_k. The self-induced EMF is then given by

$$L_k \frac{dj_k}{dt} = \oint_S \frac{\partial\vec{A}}{\partial t}\cdot\vec{\kappa}_k \, dS = \frac{dj_k}{dt}\oint_S \vec{a}_k \cdot \vec{\kappa}_k \, dS. \quad (13)$$

Note that $\vec{E} = -\partial\vec{A}/\partial t$ is the induced electric field according to Faraday's law. As can be shown, the coupling of any applied electric field to circuit k is given similarly by

$$e_k = -\oint_S \vec{E}\cdot\vec{\kappa}_k \, dS. \quad (14)$$

Further, the mutual inductance of circuits k and l is

$$M_{kl} = \oint_S \vec{a}_k \cdot \vec{\kappa}_l \, dS = \frac{\mu_0}{4\pi}\oint_S\oint_S \frac{\vec{\kappa}_k(\vec{r}) \cdot \vec{\kappa}_l(\vec{r}')}{|\vec{r}-\vec{r}'|} dS\, dS', \quad (15)$$

where the second form comes from expressing the vector potential generated by $\vec{\kappa}_k$ as $\vec{a}_k(\vec{r}) = \frac{\mu_0}{4\pi}\oint_S \frac{\vec{\kappa}_k(\vec{r}')}{|\vec{r}-\vec{r}'|} dS'$.

The mutual inductances, however, do not adequately describe the coupling between the basis functions since the eddy currents $\vec{\kappa}_k$ share the same conductor. Consider an analogy to simple electric circuits: if a resistor is shared by two electric circuits, a current in one circuit leads to a voltage across the resistor, which appears as a voltage source in the other circuit. This effect can be viewed as an additional EMF given by Eq. (14) with $\vec{E} = -\vec{K}/\sigma d$ opposing the electric field given by Ohm's law. Setting $\vec{K} = j_l\vec{\kappa}_l$, we obtain this "resistive EMF" induced in circuit k by current j_l in circuit l. To express this EMF simply as $e_k = R_{kl} j_l$, we define the *mutual resistance* of circuits k and l as

$$R_{kl} = \oint_S \frac{\vec{\kappa}_k \cdot \vec{\kappa}_l}{\sigma d} dS = \oint_S \frac{\nabla\psi_k \cdot \nabla\psi_l}{\sigma d} dS. \quad (16)$$

Equations (15) and (16) also give the self-inductance and resistance as $L_k = M_{kk}$ and $R_k = R_{kk}$.

C. Dynamics and response of eddy currents

The equation of motion for the eddy currents is found simply by requiring the total voltage around each circuit k to be zero (Kirchhoff's second law): $\sum_l (R_{kl} j_l + M_{kl} dj_l/dt + e_k) = 0$, where e_k is an externally induced EMF. If we consider R_{kl} and M_{kl} as matrix elements of $\boldsymbol{R}$ and $\boldsymbol{M}$, this becomes

$$\boldsymbol{M}\frac{d}{dt}\boldsymbol{j}(t) = -\boldsymbol{R}\boldsymbol{j}(t) - \boldsymbol{e}(t). \quad (17)$$

Here, the components of the state vector $\boldsymbol{j}$ are the currents j_k, and those of $\boldsymbol{e}$ are the EMFs e_k given by Eq. (14), where $\vec{E}$ is the electric field induced only by an applied or interfering magnetic field $\vec{B}_e$ (Faraday's law).

To obtain a more convenient form for e_k, we note that the integrand is $\vec{E}\cdot\nabla\psi_k \times \hat{n} = -\nabla\psi_k \times \vec{E}\cdot\hat{n}$, and that $\nabla\psi_k \times \vec{E} = \nabla\times(\psi_k\vec{E}) - \psi_k\nabla\times\vec{E}$. Using Stokes' theorem, the integral of $\nabla\times(\psi_k\vec{E})$ can be shown to vanish, which leads to

$$e_k = -\oint_S \vec{E}\cdot\nabla\psi_k \times \hat{n}\, dS = \oint_S \psi_k \frac{\partial\vec{B}}{\partial t}\cdot d\vec{S}, \quad (18)$$

where $\vec{B} = \vec{B}_e$ and $d\vec{S} = \hat{n}dS$.

Equation (18) also leads to an alternative form for the mutual inductances. By inserting the magnetic field from circuit l, $\vec{B}(\vec{r},t) = j_l(t)\vec{\beta}_l(\vec{r})$, and noting that $e_k = M_{lk}dj_l/dt$, we see that

$$M_{kl} = M_{lk} = \oint_S \psi_k \beta_l^{\perp}\, dS, \tag{19}$$

where $\beta_k^{\perp}$ is the normal component of the magnetic field in S produced by a unit current in circuit k.

Based on the symmetry of Eq. (15), $\boldsymbol{M}$ is Hermitian and therefore has real eigenvalues. Zero is not an eigenvalue of $\boldsymbol{M}$, since the corresponding eigenvector would be a non-zero eddy-current pattern with zero inductance, i.e., zero magnetic field everywhere. Hence, $\boldsymbol{M}$ is also invertible. Equation (17) therefore has a solution

$$\boldsymbol{j}(t) = -\int_{-\infty}^{t} e^{-(t-s)\boldsymbol{M}^{-1}\boldsymbol{R}}\boldsymbol{M}^{-1}\boldsymbol{e}(s)\, ds. \tag{20}$$

Note that the mutual inductance matrix $\boldsymbol{M}$ also directly affects the coupling of $\boldsymbol{e}$ to the system.

The Hermitian resistance matrix $\boldsymbol{R}$ is positive definite, since a negative eigenvalue would violate the second law of thermodynamics, and a zero eigenvalue can correspond only to a superconducting path. Therefore, also $\boldsymbol{R}$ is invertible for a normal-metal shield.

For simplicity, consider a shield with constant σd. If the basis is orthonormal, i.e.,

$$\oint_S \vec{\kappa}_k \cdot \vec{\kappa}_l\, dS = \oint_S \nabla\psi_k \cdot \nabla\psi_l\, dS = \delta_{kl}, \tag{21}$$

Eq. (16) leads simply to $\boldsymbol{R} = (\sigma d)^{-1}\boldsymbol{I}$. We further assume that a finite set of n circuits describes the eddy currents with sufficient accuracy.

Instead of using Eq. (20), we can now decouple the system of differential equations. The Hermitian $\boldsymbol{M}$ diagonalizes as $\boldsymbol{M} = \boldsymbol{J}\boldsymbol{L}\boldsymbol{J}^*$, where $\boldsymbol{L} = \mathrm{diag}(l_1, l_2, \ldots, l_n)$ contains the eigenvalues l_k of $\boldsymbol{M}$ and * denotes the conjugate transpose. Corresponding eigenvectors $\boldsymbol{j}_k$ form the columns of the unitary matrix $\boldsymbol{J} = \begin{bmatrix}\boldsymbol{j}_1 & \boldsymbol{j}_2 & \cdots & \boldsymbol{j}_n\end{bmatrix}$. Inserting the decomposition and $\boldsymbol{R} = (\sigma d)^{-1}\boldsymbol{I}$ into Eq. (17) and rearranging leads to a decoupled system in the eigenbasis of $\boldsymbol{M}$

$$\frac{d}{dt}[\boldsymbol{J}^*\boldsymbol{j}(t)] = -(\sigma d\boldsymbol{L})^{-1}[\boldsymbol{J}^*\boldsymbol{j}(t)] - \boldsymbol{L}^{-1}[\boldsymbol{J}^*\boldsymbol{e}(t)]. \tag{22}$$

Thus, with the substitutions $\boldsymbol{J}^*\boldsymbol{j}(t) = \tilde{\boldsymbol{j}}(t)$ and $\boldsymbol{J}^*\boldsymbol{e}(t) = \tilde{\boldsymbol{e}}(t)$, we obtain an independent ordinary differential equation,

$$\frac{d}{dt}\tilde{j}_k(t) = -\frac{1}{l_k\sigma d}\tilde{j}_k(t) - \frac{1}{l_k}\tilde{e}_k(t), \tag{23}$$

for each eddy-current mode k given by the eigenvector $\boldsymbol{j}_k$. Since these equations are exactly of the form of Eq. (1), each mode can be considered an independent LR circuit with $L = l_k$, $R = (\sigma d)^{-1}$, and a characteristic time constant $\tau_k = l_k\sigma d$. The solution of Eq. (23) is

$$\tilde{j}_k(t) = -\frac{1}{l_k}\int_{-\infty}^{t} e^{-(t-s)/\tau_k}\tilde{e}_k(s)\, ds. \tag{24}$$

D. From eddy-current modes to shielding

The eigenvectors of $\boldsymbol{M}$ are important also from a shielding point of view. In this section, we study how an MSR shields external interference, assuming $\boldsymbol{M}$ is already diagonalized ($\boldsymbol{M} = \boldsymbol{L}$, $\boldsymbol{j} = \tilde{\boldsymbol{j}}$, $\boldsymbol{e} = \tilde{\boldsymbol{e}}$) and the orthonormality condition given by Eq. (21) is satisfied.

If, in addition, the ψ_k are orthogonal in the sense that

$$\oint_S \psi_l\psi_k\, dS = 0, \text{ for } l \neq k, \text{ and } \oint_S \psi_k\, dS = 0, \tag{25}$$

the mutual inductance matrix, with elements given by Eq. (19), can be diagonal only if

$$\beta_k^{\perp} = \alpha_k\psi_k, \tag{26}$$

where α_k is a constant. This follows because $\beta_l^{\perp}$ has a representation in the ψ_k basis. Using Eq. (19), one obtains

$$\alpha_k = L_k \Big/ \oint_S \psi_k^2\, dS. \tag{27}$$

The above scenario is especially useful because any magnetic field $\vec{B}$ in V, when generated by sources not in the interior of V, is entirely determined by the normal component $B^{\perp} = \vec{B}\cdot\hat{n}$ in S. This is because the field can be expressed as $\vec{B} = -\nabla\Phi$, where the magnetic scalar potential Φ satisfies the Laplace equation $\nabla^2\Phi = 0$; when the normal derivative $\nabla\Phi\cdot\hat{n}$ has a boundary condition in S, the equation has[25] a unique solution in V. Here, the boundary condition is $\nabla\Phi\cdot\hat{n} = -B^{\perp}$. This motivates expressing the magnetic field in terms of the eddy-current basis functions ψ_k, which can be carried out separately for the external interference field $\vec{B}_{\mathrm{e}} = -\nabla\Phi_{\mathrm{e}}$ and the field $\vec{B}_{\mathrm{s}} = -\nabla\Phi_{\mathrm{s}}$ generated by eddy currents in the shield.

Within V, the applied field takes the form

$$\vec{B}_{\mathrm{e}}(\vec{r},t) = \sum_k b_k(t)\vec{\beta}_k(\vec{r}) = -\nabla\sum_k \alpha_k b_k(t)\phi_k(\vec{r}), \tag{28}$$

where ϕ_k is the solution of the Laplace equation with boundary condition $\hat{n}\cdot\nabla\phi_k = -\psi_k$ in S. The EMF induced in circuit k by $\vec{B}_{\mathrm{e}}$ is then given by

$$e_k = \alpha_k\frac{db_k}{dt}\oint_S \psi_k^2\, dS = L_k\frac{db_k}{dt}, \tag{29}$$

and the magnetic field caused by eddy currents in the shield becomes

$$\vec{B}_{\mathrm{s}}(\vec{r},t) = \sum_k j_k(t)\vec{\beta}_k(\vec{r}) = -\nabla\sum_k j_k(t)\alpha_k\phi_k(\vec{r}). \tag{30}$$

From Eq. (23) and its Fourier-transform solution [see Eq. (2)], one obtains $\hat{j}_k(\omega)$ and the scalar potential caused by the shield

$$\hat{\Phi}_s(\vec{r},\omega) = -\sum_k \alpha_k \phi_k(\vec{r})\left(1-\frac{1}{1+i\omega\tau_k}\right)\hat{b}_k(\omega), \quad (31)$$

where the time constants are $\tau_k = L_k\sigma d$. The Fourier components of the total magnetic field in V then become

$$\hat{\vec{B}}(\vec{r},\omega) = -\nabla\left[\hat{\Phi}_e(\vec{r},\omega)+\hat{\Phi}_s(\vec{r},\omega)\right] = \sum_k \frac{1}{1+i\omega\tau_k}\vec{\beta}_k(\vec{r})\hat{b}_k(\omega), \quad (32)$$

which is a low-pass-filtered version of the applied field $\hat{\vec{B}}_e$. The pass band, however, differs for components of the field that correspond to eddy-current modes with different time constants. As a result, the shielding efficiency depends not only on the frequency $f=\omega/2\pi$ but also on the spatial profile of the applied interference field; furthermore, the spatial profile is affected by the shield.

To derive Eq. (32), we assumed that the set of basis functions ψ_k yielding a diagonal inductance matrix $\boldsymbol{M}$ also satisfies Eq. (25). An example that has this property is a spherical surface S with radius R_s and the *real spherical harmonics*[26] (RSHs) forming the basis functions ψ_k. The RSHs $Y_l^m(\vec{r}) = Y_l^m(\theta,\phi)$ are expressed in terms of the usual complex spherical harmonics $\tilde{Y}_l^m(\theta,\phi)$:

$$Y_l^m = \begin{cases} 2^{-\frac{1}{2}}\left[\tilde{Y}_l^m + (-1)^m\tilde{Y}_l^{-m}\right], & m>0, \\ \tilde{Y}_l^m, & m=0, \\ 2^{-\frac{1}{2}}\left[\tilde{Y}_l^{-m} - (-1)^m\tilde{Y}_l^m\right], & m<0. \end{cases} \quad (33)$$

These functions obey the orthogonality relations

$$\oint_S Y_l^m Y_{l'}^{m'}\, dS = R_s^2\delta_{ll'}\delta_{mm'} \quad (34)$$

and

$$\oint_S \nabla Y_l^m \cdot \nabla Y_{l'}^{m'}\, dS = l(l+1)\delta_{ll'}\delta_{mm'}. \quad (35)$$

This allows the scalar basis functions to be defined as

$$\psi_l^m(\vec{r}) = \frac{1}{\sqrt{l(l+1)}}Y_l^m(\theta,\phi), \quad (36)$$

satisfying also the orthonormality given by Eq. (21). For convenience, we indexed the quantities corresponding to the modes with subscript l and superscript m (instead of a single subscript), which are integers satisfying $l \geq 1$ and $|m| \leq l$.

The corresponding magnetic field patterns $\vec{\beta}_l^m$ can be found by taking the general solution of the Laplace equation in spherical coordinates[25] within and outside V and applying boundary conditions at S. In V, one obtains

$$\vec{\beta}_l^m(\vec{r}) = \frac{\mu_0}{2R_s^l}\frac{l+1}{2l+1}\nabla r^l Y_l^m(\theta,\phi), \quad (37)$$

which leads to self-inductances

$$L_l^m = \frac{\mu_0 R_s}{2l+1} \quad (38)$$

and zero mutual inductances. There is no dependence on m, i.e., the eigenvalues of the inductance matrix are $(2l+1)$-fold degenerate. The value for α_l^m is found to be $\frac{\mu_0 l(l+1)}{R_s(2l+1)}$. The corresponding time constants are

$$\tau_l^m = \frac{\mu_0 R_s\sigma d}{2l+1}, \quad (39)$$

identical to a result obtained from a different approach elsewhere.[27] The time constants can be used in Eq. (32) to obtain the residual field inside the MSR from the external interference field $\vec{B}_e$. The expansion coefficients $b_l^m(t)$ can be obtained from

$$b_l^m(t) = \frac{R_s(2l+1)}{\mu_0\sqrt{l(l+1)}}\oint_S Y_l^m(\theta,\phi)\vec{B}_e(\vec{r})\cdot d\vec{S}. \quad (40)$$

Similarly, the coefficients can be calculated for a field applied from inside the MSR, since the eddy currents simply respond to the normal component of the magnetic field at the shield, regardless of the source. This allows one to study how the MSR distorts applied magnetic fields.

The spherical-shield example also reveals the effect of MSR size on transients and shielding: increasing R_s lengthens the time constants and improves shielding while strongly reducing the coupling from the pulsed coil to the MSR and from the eddy currents to the sample volume.

E. Rectangular shielded room

The theory for eddy currents can be applied to thin conducting shields with different geometries or even multiple layers. After parameterizing or discretizing the shielding surfaces, one can analyze eddy currents using linear algebra and surface integrals. While the simple spherical model discussed above can be very helpful in understanding eddy currents in MSRs in general, most practical shields are rectangular.

In Sec. IV, we describe a cubic MSR constructed of rectangular plates which are intentionally connected only weakly to each other. The plate-to-plate boundaries are low-conductivity regions of the surface S which affect the dynamics of the eddy currents through the resistance matrix $\boldsymbol{R}$. There is a difficulty, however, in that the integrand in Eq. (16) becomes nearly singular at the plate boundaries. Another problem when σd is allowed to vary within S is that the system matrix $\boldsymbol{M}^{-1}\boldsymbol{R}$ in general becomes non-Hermitian, making the analysis more complex both numerically and conceptually.

If we assume the boundaries to be fully disconnected, however, these difficulties can be circumvented by selecting a basis for Ψ that is restricted to current patterns that do not cross the plate boundaries. This restriction is equivalent to Ψ being constant along boundaries, i.e., $\vec{K} = \nabla\Psi\times\hat{n}$ has no component perpendicular to boundaries. For convenience, we assume that, within all the boundaries in S, there is a path between any two boundary points. This implies that, at all

boundaries, Ψ has the same value, which we define to be zero.

One practical basis that satisfies this requirement for a single rectangular plate of dimensions $w \times h$ is a two-dimensional Fourier basis consisting of the functions

$$\psi_{nm}(x,y) = \frac{\sin\left(\frac{n\pi x}{w}\right)\sin\left(\frac{m\pi y}{h}\right)}{\frac{\pi}{2}\sqrt{wh\left(\frac{n^2}{w^2}+\frac{m^2}{h^2}\right)}}, \tag{41}$$

where $0 \le x \le w$, $0 \le y \le h$, and n and m are positive integers. Any function in the plate that is piecewise continuous, and zero at the edges, has a representation in this basis. Similar basis functions assigned to each plate in an MSR thus represent all possible eddy-current patterns.

As is straightforward to show, a basis so defined satisfies the orthonormality condition given by Eq. (21). Therefore, if σd is constant and identical for each plate, the resistance matrix becomes $\boldsymbol{R} = (\sigma d)^{-1}\boldsymbol{I}$, and $\boldsymbol{M}^{-1}\boldsymbol{R} = (\sigma d\boldsymbol{M})^{-1}$ is Hermitian. As described in Sec. III C, the system can now be decoupled into simple single-variable differential equations [Eq. (23)] by switching to the eigenbasis of $\boldsymbol{M}$. Subsequently, it is straightforward to find the response of the MSR to any applied field.

In practice, the values for the order indices n and m must be chosen to extend from unity to a number that produces sufficient detail in the eddy-current patterns. The inductances decrease with increasing n and m, so that including higher-order basis functions adds short time constants to the system, making the matrix $\boldsymbol{M}$ increasingly ill-conditioned. The upper values of m and n are thus chosen sufficiently high to provide accurate representations of the eddy currents, but not so high as to generate numerical instability.

The eddy-current model is especially efficient for analyzing unwanted transients, since the number of basis functions required to describe the essential properties of the transients is relatively small, with n and m not necessarily exceeding 10 or even 5. The sine-function basis additionally allows the use of the 2-D Fast Fourier Transform (FFT) for efficient calculation of, e.g., the surface integral of Eq. (19). In Sec. VI, we present numerical results in which we evaluate Eq. (24) after computing the elements of $\boldsymbol{M}$ and calculating its eigenvalue decomposition in Matlab. We used a total of 1536 eddy-current basis functions, although as few as 96 were sufficient to capture the essential properties of the transient field. The polarizing coil was modeled as a vertically oriented point dipole at the center of the MSR with a magnitude determined by the calculated dipole moment.

F. Higher modes and frequencies

Despite the associated computational difficulties, adding higher-order values of n or m raises interesting issues from a theoretical point of view. When one sums contributions from all basis functions up to infinite order, although Ψ must always be zero at the boundaries, one can nonetheless describe any eddy current pattern. This is because Ψ can converge to a nonzero value arbitrarily close to a boundary line, resulting in a discontinuity in Ψ at the boundary and to a delta function in the component of $\nabla\Psi$ perpendicular to the boundary. This, in turn, corresponds to a current within the boundary line. If Ψ has the same nonzero value in the plate on the other side of the slit, the two currents will be equal and opposite, effectively canceling each other out. Consequently, the net current may contain currents that appear to cross the boundaries.

With increasing frequency, the behavior of the eddy-current model thus approaches that of a perfect (or superconducting) shield. The validity of the model, however, breaks down at frequencies high enough that we can no longer neglect the displacement current. Furthermore, for basis functions of sufficiently high order, the shield is no longer thin compared to the length scales present in the eddy-current patterns. The thin-shield approximation also breaks down because of the skin effect—the fact that, at high frequencies, the current flows mostly within a skin depth of the surface of the conductor. This non-uniformity in the current across the thickness of the plates modifies the effective resistance of the eddy-current circuits. One approach to solving this problem may be to model the plates with a number of thin sheets with spacings smaller than the skin depth. However, to justify this simplification theoretically, one should study whether significant currents can flow perpendicularly to the plates, i.e., from one layer to another. This nontrivial task is left for future work.

IV. DESIGN AND CONSTRUCTION OF NEW SHIELDED ROOM

As discussed in Sec. III, the shielding is determined largely by the time constants of the eddy-current modes in the conducting MSR. The relevant modes depend on the position and nature of the noise sources as well as on the detector. As the details of the sources are mostly unknown, we designed the shield so that the estimated eddy-current transient would be just short enough to allow NMR measurements to begin approximately 15 ms after the 10-ms ramp-down of B_p is completed. This would allow measurements of tissues or samples with NMR T_1 relaxation times on the order tens of milliseconds or larger.

The time constants in the shield can be shortened in two ways. First, decreasing the thickness of the shield increases the resistance of the eddy-current circuits, thereby shortening the time constants although at the expense of the shielding performance. Second, using disconnected metal plates reduces the sizes, and therefore inductances, of the effective current loops, replacing the modes with the longest time constants with ones with shorter time constants. Given that the entrance door already introduces weak connections between plates and that the resistances of connections at the edges of the cube are difficult to control, we implemented both approaches.

The new cubic MSR [Fig. 2(a)] has the same dimensions as its predecessor. Based on measurements of the current paths (Secs. V and VI) and computed estimates of how the transient amplitudes and time constants scale with plate

dimensions, we chose the thickness to be 1.6 mm (1/16″), a quarter of that of the old shielded room. The resistivity of 6061 aluminum alloy is[28] $1/\sigma = 3.7 \times 10^{-8}\,\Omega$m.

To maintain a high level of symmetry, we divided each of the four sides into individual plates in the same way as the front wall, containing the door in the middle [see Fig. 2(b)]. Priority was given to the symmetry for two reasons. First, if subsequently one wished to reduce the transient further by means of actively driven compensation coils (or *dynamical cancellation*,[16] developed subsequently), this would be much easier in a highly symmetric room. With a B_p coil centered and aligned with the room, the transient is homogeneous to first order at the center. Such a field can be compensated to a high accuracy in a small volume by using just one compensation coil. On the other hand, a transient from an asymmetric room with its complicated spatio-temporal profile can be difficult even to analyze. Second, asymmetric shields are more likely to reduce the benefit of the gradiometer by converting uniform magnetic fields into gradients, as discussed in Sec. III, resulting in increased interference.

We also explicitly chose not to divide the wall plates by a horizontal seam. As follows from the theory in Sec. III and will be evident from the results in Sec. VI, the transient eddy currents induced by the vertical polarizing field do not cross the horizontal symmetry plane. Therefore, a division along that plane would not reduce the transient, but merely impair the shielding. However, two horizontal division planes placed symmetrically above and below the middle plane would reduce the transient. At the four corners of the room, we would have preferred to use bent (L-shaped) plates rather than vertical seams, but were unable to bend the large plates.

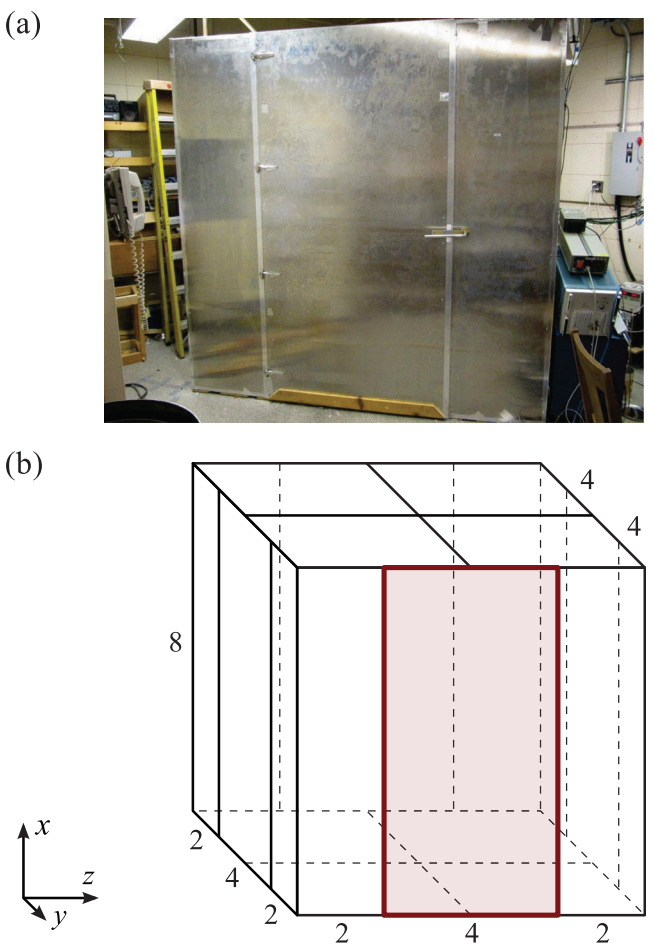

FIG. 2. New low-eddy-current MSR with dimensions $2.4 \times 2.4 \times 2.4\,\text{m}^3$ ($8^3\,\text{ft}^3$). (a) Photograph and (b) configuration of 1.6-mm aluminum plates (dimensions in feet = 0.3048 m; shaded rectangle is the door).

To keep the plates electrically separated, the supporting frame was made of wood with a square cross section of 38×38 mm^2. The metal sheets, with dimensions shown in Fig. 2(b), were bolted edge-to-edge to the frame, with adhesive tape between them to prevent direct electrical contact. To make the shield effective against RF interference, the narrow slits between plates were covered with aluminum-foil adhesive tape. To maintain symmetry, aluminum-foil tape with a conducting adhesive was used to cover the corner seams as well as the seams dividing the ceiling and floor. Before applying the tape, we cleaned the tarnished surfaces using acetic-acid solution and isopropanol. The remaining vertical seams were covered using tape with a non-conductive adhesive.

The door plate, which was suspended on four heavy-duty stainless-steel hinges, was RF sealed using a commercial EMI gasket—a strip of rubber foam covered with conducting fabric—attached to the outside of the door frame. The door, which is somewhat larger than the opening, closes to the outside of the door frame. An external clamp maintains a modest pressure on the gasket, providing an RF seal around the entire perimeter of the door. As in the previous MSR,[29] hoses for water and helium gas are passed through the walls via metal pipes that behave as "waveguides beyond cutoff," attenuating electromagnetic waves with wavelengths larger than twice the pipe diameter.

V. METHODS FOR MEASURING TRANSIENT FIELDS AND EDDY-CURRENT MAPS

We measured the transient eddy-current patterns in the walls and the magnetic fields at the imaging target at the center of the room in both the previous and new MSR using the techniques described below.

A. Transient-field study

The SQUID-based gradiometer was not a suitable instrument to measure the transient magnetic *field*. For the 6.4-mm room, we used instead a three-axis, APS 520A fluxgate magnetometer, placed at the center of the MSR. Because a 150-mT polarizing pulse would leave the fluxgate core magnetized, we reduced the amplitude of the 300-ms polarizing pulse to 0.0113 mT. The field was turned off in 10 ms, mimicking the turn-off ramp of the full 150-mT pulse. Subsequently, we recorded the fluxgate signal generated by the eddy-current transient.

In the case of the 1.6-mm MSR, however, the transient response was much lower and swamped by transients from the fluxgate. Thus, we assembled a dedicated SQUID magnetometer using a superconducting flux transformer made from insulated NbTi wire. The circular 25-mm pickup loop was coupled to a three-turn coil placed next to and in the plane of the SQUID, inside its cylindrical Nb shield. The measurable

field range was about 0.1 mT. In this case we applied 0.013-mT pulses, again with a 10-ms turn-off time. To eliminate line-frequency harmonics and low-frequency noise, we averaged each data set over 1000 acquisitions.

For both MSRs, we disconnected the power supply from the polarizing coil at the end of the pulse using a reed relay. The measured values were scaled linearly to correspond to 150-mT polarizing pulses, assuming that the eddy currents scale linearly with the applied magnetic fields. We compared our experimental data with predictions based on the theory described in Sec. III E.

B. Eddy-current patterns

We determined the severity of the MSR transient problem by measuring the magnetic field, as described above. To understand the problem more thoroughly, however, we also mapped the eddy currents as a function of time by measuring the magnetic field both inside and outside the MSR wall. Since the wall is thin, the current is described by a tangential surface current density $\vec{K}$. We calculated values of $\vec{K}$ from the discontinuity of the magnetic field across the wall, using the expression

$$\vec{K} = \frac{1}{\mu_0}\,\hat{n} \times (\vec{B}_+ - \vec{B}_-), \tag{42}$$

which follows from the quasistatic boundary condition over a surface surrounded by a free-space-like medium, $\vec{B}_+ - \vec{B}_- = \mu_0 \vec{K} \times \hat{n}$ (see Sec. III A).

Since the sensor placed at the wall was exposed to only a fraction of the polarizing pulse, it was possible to use the APS 520A fluxgate magnetometer for both MSRs with 150-mT pulses. We measured the field in three orthogonal directions on a grid of points marked on both sides of the wall; the two grids were carefully aligned. The thickness of the fluxgate enclosure was 25 mm, which we added to the wall-plate thickness to determine the separation of the measurement points on opposite sides of the wall. To obtain accurate estimates of the surface current, the separation of each pair of measurement points must be small compared to the sizes of other conductors or other sources nearby. Each final measurement point was an average of four repetitions to reduce the effects of line-frequency interference.

The theoretical model in Sec. III E was used to calculate the eddy-current patterns in the new MSR.

VI. RESULTS

Figure 3 shows the transient magnetic fields following the polarizing pulse, measured at the center of the 6.4-mm and 1.6-mm rooms. The field magnitudes are scaled to a polarizing pulse of 150 mT. Time is defined with $t = 0$ at the end of the B_p ramp-down. It is immediately evident that the field transient is enormously lower in the 1.6-mm room compared with the 6.4-mm room. At $t = 15$ ms (out of range in Fig. 3), the transient field in the 6.4-mm MSR is 190 μT, and at $t = 30$ ms, the eddy currents are still strong enough to produce a field larger than B_0. Since the field transient is perpendicular to $\vec{B}_0 = B_0 \hat{e}_z$, the total field is rotated by more than

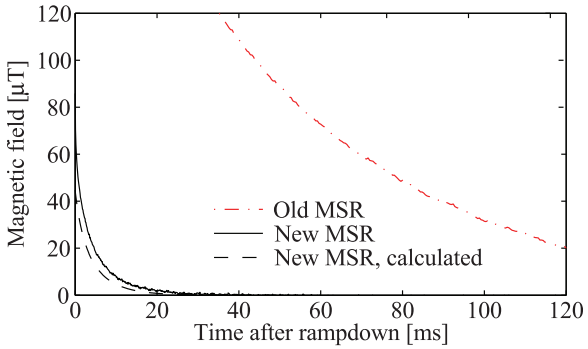

FIG. 3. The x component of the MSR eddy-current field at the sample after pulsing $\vec{B}_p = B_p \hat{e}_x$ at the center of the MSR in the old and new rooms. Other components are small. Time is measured from the end of the 10-ms ramp-down. The field is scaled to correspond to a 150-mT pulse.

45° from the z axis. The longest time constant of the decaying transient, 50 ms from an exponential fit, is comparable with T_1 times of soft tissues.[30] The ULF MRI system cannot be operated under these conditions: by the time the eddy currents have decayed sufficiently, the signal will have largely disappeared.

For the 1.6-mm MSR, a similar fit gave a dominant time constant of 6.0 ms. At 15 ms after ramp-down, the measured transient has decayed to about 4 μT along the x axis, giving a total field magnitude of $\sqrt{132^2 - 4^2}$ μT = 132.06 μT. The change from $B_0 = 132$ μT is approximately one part in 2000, corresponding to a frequency shift of 3 Hz. This is on the same order as the inhomogeneous broadening of the NMR peak of some tissues[30] and from an imaging point of view therefore has little effect. At 20 ms, the transient is negligible. The calculated transient magnitude is slightly smaller than the measured field. The difference is potentially due to small currents that cross plate boundaries or another transient effect that causes a measurement error. However, the two longest time constants in the simulated transient are 5.8 and 6.9 ms; the former has the higher amplitude and is remarkably close to the measured value.

Eddy-current patterns in three of the six faces of the 6.4-mm MSR were mapped as a function of time and are shown at two different times in Fig. 4. At $t = 2$ ms, the eddy current densities are on the order of 400 A/m. By integrating across the measurement points, we found that a current of about 1 kA circulates horizontally around the MSR. The currents in the front wall are quite similar to those in the left wall, despite the presence of the door which adds a significant resistance along the current paths. We observe that the currents in the ceiling are reasonably symmetric about the center. This is in agreement with the discussion of higher-order modes in Sec. III F.

During the decaying transient, the surface-current patterns change significantly. This is because the polarizing pulse excites multiple eddy-current modes that decay with their individual time constants. Notably, the large current across the front wall decays quickly, leaving two small current loops circulating inside the door plate in opposite directions. In the remainder of the wall, the currents flow around the door to pass through the ceiling and floor. Similarly, in the ceiling the current is concentrated near the front wall.

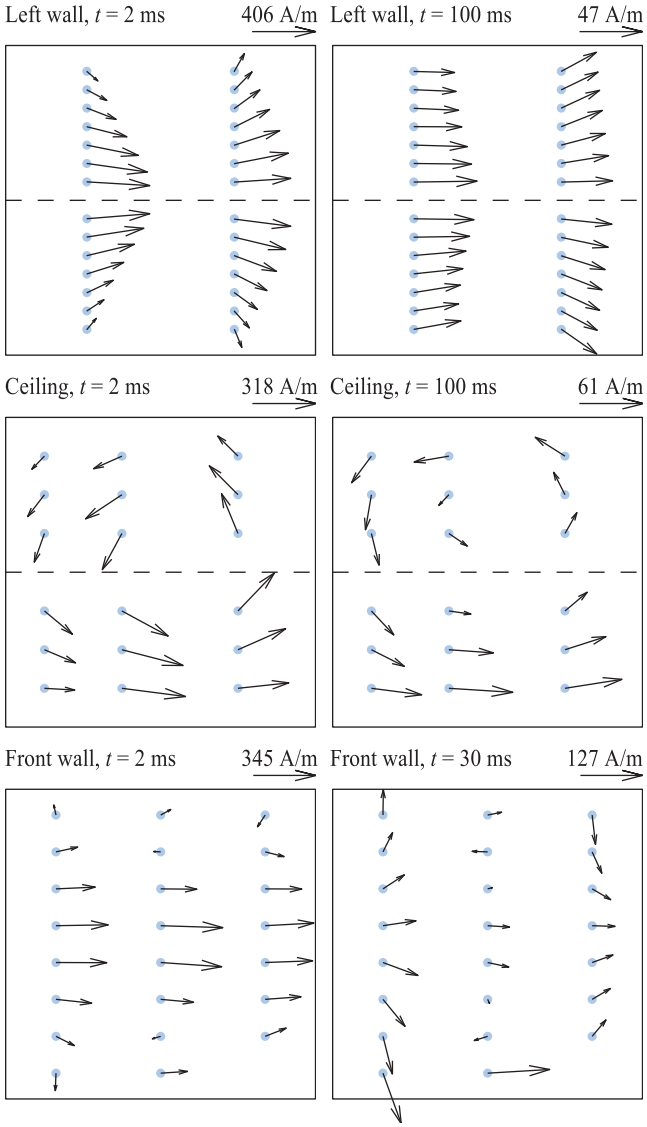

FIG. 4. Surface eddy-current densities at time t after ramp-down of $\vec{B}_p = B_p\hat{e}_x$ pulsed at the center of the old MSR. The measurements are from the left wall, ceiling, and front wall of the MSR [the orientations correspond to Fig. 1(c)]. The values are scaled to correspond to a 150-mT pulse.

Even in the left wall, the currents begin to spread up and down to avoid the door. The asymmetry caused by the door seemingly shifts the effective "axis of rotation" of the currents towards the rear of the MSR.

With time, the currents in the left wall become more evenly spread across the entire height. In the simplest case, this can be explained by a combination of two modes-one nearly uniform mode around the entire cube with a long time constant, and a second consisting of current loops within the individual plates. The current loops are counterclockwise above the horizontal symmetry plane and clockwise below it. This follows from the directions in which the magnetic flux lines from the polarizing pulse penetrate the MSR wall. The fact that the current around the whole cube decays more slowly is evidence of the low resistance of plate-to-plate connections as well as the larger inductance.

Similar measurements for the 1.6-mm MSR were carried out while most of the MRI instrumentation was not inside. The largely unobstructed access to both sides of the wall allowed us to use a finer grid. Fig. 5 shows the measured eddy-current density (black) at $t = 2$ ms along with the calculated result (red).

As the plates become effectively disconnected from each other at these time scales, only currents circulating inside the individual plates are large enough to be seen in the data. The current circulating around the entire room has been suppressed to the point that we cannot detect it. Qualitatively, the patterns in the 1.6-mm room change very little over time, and the measured currents in the middle plates decay with a time constant of 6 ms, in excellent agreement with the measured field transient at the center of the room. This means that the eddy currents are composed predominantly of modes with time constants close to 6 ms. The measured and calculated eddy-current patterns are also strikingly similar; the arrows overlap almost perfectly. Similar agreement was found at other times.

While the eddy-current magnitudes at $t = 2$ ms are only about a factor of two lower than in the 6.4-mm room, the field transient especially at later times is substantially lower because of the shorter decay times and the more localized eddy-current loops. Finally, as mentioned in Sec. IV, the currents do not cross the horizontal middle plane. Hence, dividing the plates along this plane would not have decreased the transient but merely degraded the shielding.

VII. CONCLUSIONS AND OUTLOOK

The problem of eddy currents induced in a thin conducting shield by a pulsed magnetic field was analyzed in detail. A theoretical model was derived to gain an intuitive understanding of eddy currents and to compute their excitation and decay dynamics accurately and efficiently. For the simple case of a spherical shield, the theory provides analytical expressions for shielding performance and transients, revealing, for instance, the benefits of large MSR size. Other geometries require numerical computation. The use of a Fourier-type basis for the surface currents, however, makes the computation very efficient, since a relatively small number of basis functions is required for the transient analysis. After deriving the theory, we became aware of recent work by Poole *et al.*[31] that describes a similar model for eddy-current analysis in a cylindrical geometry.

The ULF MRI system was upgraded to function with a larger, water-cooled polarizing coil for *in vivo* studies. We described the new MSR, which consists of weakly connected 1.6-mm aluminum plates in a highly symmetric geometry. Compared with the previous MSR, with tightly connected 6.4-mm plates, the new configuration reduced the unwanted field transient by two orders of magnitude at 15 ms after B_p ramp-down. This substantial improvement made it possible to use 150-mT pulses with the new polarizing coil. The new coil allows the positioning of a human head in the imaging volume; the effective imaging volume is now determined by the depth sensitivity of the gradiometer.

We presented experimental procedures for measuring eddy-current transients and, in particular, eddy-current vector maps. These maps revealed a total induced current on the

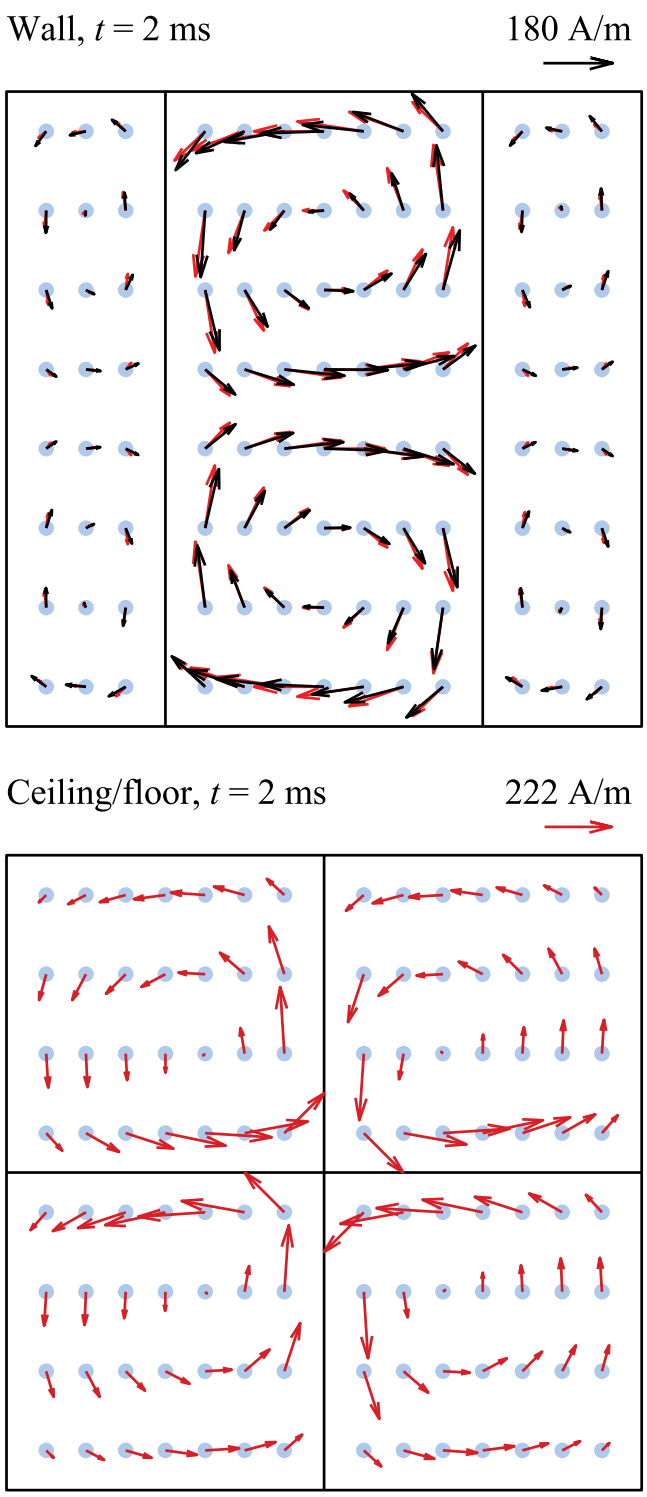

FIG. 5. Surface eddy-current densities with $\vec{B}_p = B_p \hat{e}_x$ pulsed at the center of the 1.6-mm MSR. Black arrows are from measurements and red arrows represent computations. The values are scaled to correspond to a 150-mT pulse.

order of 1 kA circulating around the old 6.4-mm MSR after a 150-mT polarizing pulse. A further finding was the substantial asymmetry in the eddy currents caused by the door. In the new MSR, however, the eddy-current patterns reflect the high level of symmetry in the design. These patterns are in remarkably good agreement with those obtained from the computational model, indicating that both the model and the measurement were successfully implemented. Consequently, any small difference between the measured and calculated magnetic-field transients in the imaging volume is likely to be due to the measurement system—for example, a dewar with metallic parts—or from the environment—for example, steel bars in the floor—rather than from the MSR walls.

As a final remark, we solved the MSR eddy-current problem with a purely passive approach, in essence, by trading shielding efficiency for lower eddy currents. Indeed, if no low-frequency measurements (< 1 kHz), such as MEG, need to be performed in the MSR, a very modest amount of shielding may be sufficient. Interestingly, it may, on one hand, be possible to operate a high-sensitivity ULF MRI scanner in the kHz range without an MSR, using gradiometric sensors with a high tolerance for RF interference. On the other hand, using partially overlapping μ-metal—and possibly aluminum—plates with weakened electrical contacts, the passive approach introduced here may allow high shielding factors even at low frequencies. Alternatively, one could use an active method, such as *dynamical cancellation*,[16] in which specially designed waveforms are fed into an additional coil, providing flexible eddy-current reduction. A combination of active and passive methods might be very effective.

ACKNOWLEDGMENTS

We are grateful to Steven Conolly for providing the water-cooled polarizing coil used in the system. We thank Matthew Nichols and Kevin Lee for technical assistance. This research was supported by the National Institutes of Health Award No. 5R21CA1333338 and by the Donaldson Trust. This work also received funding from the Academy of Finland, from the Finnish Cultural Foundation and from the European Community's Seventh Framework Programme (FP7/2007–2013) under Grant Agreement No. 200859.

[1]Z.-P. Liang and P. C. Lauterbur, *Principles of Magnetic Resonance Imaging: A Signal Processing Perspective, IEEE Press Series in Biomedical Engineering* (IEEE Press, Piscataway, NJ, USA, 2000).
[2]R. McDermott, S. Lee, B. ten Haken, A. H. Trabesinger, A. Pines, and J. Clarke, Proc. Natl. Acad. Sci. U.S.A. **101**, 7857 (2004).
[3]S. K. Lee, M. Mößle, W. Myers, N. Kelso, A. H. Trabesinger, A. Pines, and J. Clarke, Magn. Reson. Med. **53**, 9 (2005).
[4]J. O. Nieminen, K. C. J. Zevenhoven, P. T. Vesanen, Y.-C. Hsu, and R. J. Ilmoniemi, Magn. Reson. Imaging **32**, 54 (2014).
[5]P. T. Vesanen, J. O. Nieminen, K. C. J. Zevenhoven, Y.-C. Hsu, and R. J. Ilmoniemi, "Current-density imaging using ultra-low-field MRI with zero-field encoding," Magn. Reson. Imaging (in press).
[6]P. T. Vesanen, K. C. J. Zevenhoven, J. O. Nieminen, J. Dabek, L. T. Parkkonen, and R. J. Ilmoniemi, J. Magn. Reson. **235**, 50 (2013).
[7]M. Burghoff, H.-H. Albrecht, S. Hartwig, I. Hilschenz, R. Körber, N. Höfner, H.-J. Scheer, J. Voigt, L. Trahms, and G. Curio, Appl. Phys. Lett. **96**, 233701 (2010).
[8]S.-J. Lee, K. Kim, C. S. Kang, S.-M. Hwang, and Y.-H. Lee, Supercond. Sci. Technol. **23**, 115008 (2010).
[9]V. S. Zotev, A. N. Matlachov, P. L. Volegov, H. J. Sandin, M. A. Espy, J. C. Mosher, A. V. Urbaitis, S. G. Newman, and R. H. Kraus, Jr., IEEE Trans. Appl. Supercond. **17**, 839 (2007).
[10]P. T. Vesanen, J. O. Nieminen, K. C. J. Zevenhoven, J. Dabek, L. T. Parkkonen, A. V. Zhdanov, J. Luomahaara, J. Hassel, J. Penttilä, J. Simola *et al.*, Magn. Reson. Med. **69**, 1795 (2013).
[11]*The SQUID Handbook*, edited by J. Clarke and A. I. Braginski (Wiley-VCH Verlag GmbH & Co. KGaA, Weinheim, Germany, 2004).

[12]P. E. Magnelind, J. J. Gomez, A. N. Matlashov, T. Owens, J. H. Sandin, P. L. Volegov, and M. A. Espy, IEEE Trans. Appl. Supercond. **21**, 456 (2011).
[13]J. O. Nieminen, P. T. Vesanen, K. C. J. Zevenhoven, J. Dabek, J. Hassel, J. Luomahaara, J. S. Penttilä, and R. J. Ilmoniemi, J. Magn. Reson. **212**, 154 (2011).
[14]S.-M. Hwang, K. Kim, C. S. Kang, S.-J. Lee, and Y.-H. Lee, Appl. Phys. Lett. **99**, 132506 (2011).
[15]S.-M. Hwang, K. Kim, C. S. Kang, S.-J. Lee, and Y.-H. Lee, J. Appl. Phys. **111**, 083916 (2012).
[16]K. C. J. Zevenhoven, "Solving transient problems in ultra-low-field MRI," Master's thesis (Aalto University, Espoo, Finland).
[17]W. Ruder, Proc. IRE 30, 437 (1942).
[18]J. E. Zimmerman, J. Appl. Phys. **48**, 702 (1977).
[19]D. Cohen, Rev. Phys. Appl. (Paris) **5**, 53 (1970).
[20]H. C. Seton, J. M. S. Hutchison, and D. M. Bussell, Cryogenics **45**, 348 (2005).
[21]N. Matter, G. Scott, T. Grafendorfer, A. Macovski, and S. Conolly, IEEE Trans. Med. Imaging **25**, 84 (2006).
[22]G. K. Batchelor, *An Introduction to Fluid Mechanics* (Cambridge University Press, 1967).
[23]R. Turner, Magn. Reson. Imaging **11**, 903 (1993).
[24]This leads to a mathematically convenient normalization of the basis functions. Another sensible normalization would be based on the total current flowing in the eddy-current loops, which can be more intuitive at least for simple eddy-current patterns.
[25]J. D. Jackson, *Classical Electrodynamics*, 3rd ed. (John Wiley & Sons, New York, USA, 1999).
[26]E. T. Whittaker and G. N. Watson, *A Course of Modern Analysis*, 4th ed. (Cambridge University Press, New York, USA, 1927).
[27]P. T. Vesanen, J. O. Nieminen, K. C. J. Zevenhoven, J. Dabek, J. Simola, and R. J. Ilmoniemi, IEEE Trans. Magn. **48**, 53 (2012).
[28]See http://www.efunda.com/ for "AA6061" from Engineering Fundamentals (eFunda).
[29]M. J. Hatridge, "SQUID magnetometry from nanometer to centimeter length scales," Ph.D. thesis (University of California, Berkeley, 2010).
[30]V. S. Zotev, A. N. Matlashov, I. M. Savukov, T. Owens, P. L. Volegov, J. J. Gomez, and M. A. Espy, IEEE Trans. Appl. Supercond. **19**, 823 (2009).
[31]M. Poole, H. Sanchez Lopez, O. Ozaki, H. Kitaguchi, I. Nakajima, S. Urayama, K.-I. Sato, H. Fukuyama, and S. Crozier, IEEE Trans. Appl. Supercond. **21**, 3592 (2011).